



# Higher photocatalytic removal of organic pollutants using pangolin-like composites made of 3–4 atomic layers of MoS<sub>2</sub> nanosheets deposited on tourmaline

Ming Hao<sup>1,2</sup> · Hao Li<sup>3</sup> · Li Cui<sup>1,2</sup> · Wei Liu<sup>4</sup> · Baizeng Fang<sup>5</sup> · Jinsheng Liang<sup>1,2</sup> · Xinlei Xie<sup>1,2</sup> · Dongxu Wang<sup>1,2</sup> · Fei Wang<sup>1,2</sup>

Received: 20 December 2020 / Accepted: 5 April 2021 / Published online: 4 May 2021  
© The Author(s), under exclusive licence to Springer Nature Switzerland AG 2021

## Abstract

Environmental pollution by organic pollutants is a serious concern which may be solved by photocatalytic degradation of pollutants, yet the efficiency of actual photocatalytic materials is limited. For instance, conventional MoS<sub>2</sub> nanosheets tend to agglomerate, which hinders the access of pollutants to active sites. To overcome this challenge, we hypothesized that assembling MoS<sub>2</sub> nanosheets on a mineral support would improve access to active sites. We synthesized a catalyst made of 3–4 atomic layers of MoS<sub>2</sub> nanosheets deposited on tourmaline using a microwave hydrothermal method. Results show that tourmaline occurs as a polyhedron single crystal that supports the epitaxial growth of 2H-MoS<sub>2</sub> layers on tourmaline (773) facets, while an intrinsic rolling up behavior of MoS<sub>2</sub> layer from [002] to [106] on the mineral surface accounts for the curly morphology. The pangolin-like MoS<sub>2</sub>/tourmaline composite degrades rhodamine B much better than the pure MoS<sub>2</sub> nanosheets assembled microspheres. This is explained by the reduced thickness of MoS<sub>2</sub> nanosheets according to the density functional theory. Overall, our findings represent a new tactic for the cost-effective batch preparation of two-dimensional materials with high catalytic performance.

**Keywords** Natural minerals · Tourmaline · Molybdenum disulfide · Microwave hydrothermal · Epitaxial growth · Photocatalysis

## Introduction

With the development of industry, excessive discharge of organic wastewater has become one of the most serious environmental problems around the world, which poses a

significant threat to environment and human health due to its persistence and toxicity (Saravanan et al. 2021; Madima et al. 2020; Mecha. et al. 2020). At present, photocatalysis as a simple and economical method has been widely used to remove organic pollutants from wastewater (de Lima et al. 2020; Saeed et al. 2018). Compared with the common photocatalyst containing TiO<sub>2</sub> and CdS, molybdenum sulfide

Ming Hao and Hao Li are contributed equally to this study.

✉ Fei Wang  
wangfei@hebut.edu.cn

Wei Liu  
weiliu@dicp.ac.cn

Baizeng Fang  
bfang@chbe.ubc.ca

Jinsheng Liang  
liangjinsheng@hebut.edu.cn

<sup>1</sup> Key Laboratory of Special Functional Materials for Ecological Environment and Information, Ministry of Education, Hebei University of Technology, Tianjin 300130, China

<sup>2</sup> Institute of Power Source and Ecomaterials Science, Hebei University of Technology, Tianjin 300130, China

<sup>3</sup> Department of Physics, Technical University of Denmark, 2800 Kongens Lyngby, Denmark

<sup>4</sup> Dalian National Laboratory for Clean Energy, Dalian Institute of Chemical Physics, Chinese Academy of Sciences, Dalian 116023, China

<sup>5</sup> Department of Chemical & Biological Engineering, University of British Columbia, 2360 East Mall, Vancouver, BC V6T 1Z3, Canada

(MoS<sub>2</sub>), a typical layered two-dimensional semiconductor material, has received considerable attention in the photo-degradation of organic pollutants due to its strong visible light response, layered structure, and environment-friendly nature (Gan et al. 2020; Wang and Mi 2017). However, due to its high specific surface energy, nanostructured MoS<sub>2</sub> suffers from aggregation inevitably which causes rapid recombination of electron–hole pairs and thus poor catalytic performance (Qu et al. 2013). One effective solution is to disperse the MoS<sub>2</sub> on support materials, such as graphene (Kumar et al. 2019), graphitic carbon nitride (Liu et al. 2018), reduced graphene oxide (Sun et al. 2017), titanium dioxide (Zhao et al. 2019), and Bi<sub>2</sub>MoO<sub>6</sub> (Li et al. 2018). However, the high preparation cost and the problematic environmental load limit these fabrication approaches from industrial applications. It becomes practically important that the MoS<sub>2</sub> nanostructures with few layers and full of active sites could be stably assembled on a support of highly natural abundance, e.g., minerals. Mineral carriers own merits of low-cost and environmental benignity (Wang et al. 2021; Hao et al. 2021; Saja et al. 2020), making them as promising candidates as a functional support. However, only few studies have focused on the fabrication of MoS<sub>2</sub> nanostructures using mineral supports, especially tourmaline. Tourmaline-supported MoS<sub>2</sub> is believed to be structurally beneficial to provide more active sites via good assembly flexibility based on its unique characteristics including spontaneous polarization and far infrared radiation.

Tourmaline is a borosilicate mineral with the R<sub>3m</sub> space group (Guerra et al. 2012) and the chemical formula of XY<sub>3</sub>Z<sub>6</sub>Si<sub>6</sub>O<sub>18</sub>(BO<sub>3</sub>)<sub>3</sub>W<sub>4</sub>, where X is Na<sup>+</sup>, Ca<sup>2+</sup>, K<sup>+</sup>, or vacancies; Y is Mg<sup>2+</sup>, Mn<sup>2+</sup>, Fe<sup>2+</sup>, Al<sup>3+</sup>, Fe<sup>3+</sup>, Mn<sup>3+</sup>, or Li<sup>+</sup>; Z is Al<sup>3+</sup>, Fe<sup>3+</sup>, Cr<sup>3+</sup>, or Mg<sup>2+</sup>; and W is OH<sup>-</sup>, F<sup>-</sup>, or O<sup>2-</sup>. It has been extensively studied due to the spontaneous and permanent poles which can produce an electric dipole (Zhou et al. 2018). Moreover, the strong electric field formed on the tourmaline surface can accelerate the separation/transportation of photoexcited charge carriers (Li et al. 2015). Besides, other unique properties such as pyroelectric, piezoelectric, and far infrared radiation have made tourmaline flexible in various fields (Zhang et al. 2014). Therefore, tourmaline owns not only the merits of the low cost but also several unique properties compared with some common carbon materials including carbon powder, biochar, and carbon nanotubes (Xu et al. 2020, 2019, 2016). In our previous studies, tourmaline has been found to effectively decrease agglomeration of silica hollow microspheres (Wang et al. 2017), as well as the nanoparticle's size (Zhang et al. 2017a). In addition, our previous study was successful in fabricating a FeMnTiO<sub>x</sub> catalyst synergized with tourmaline support for low-temperature NH<sub>3</sub>-SCR (Wang et al. 2019). These works serve as direct evidence that tourmaline can be used to improve catalytic activity. In this work, using

a one-step microwave hydrothermal method, we report the first preparation of an ingenious MoS<sub>2</sub>/tourmaline composite composed of atomically few layered MoS<sub>2</sub> nanosheets growing along the surface of tourmaline particles. This structure significantly increases the dispersion of MoS<sub>2</sub> nanosheets and provides more active sites for catalysis. The spontaneous polarization and far infrared radiation of tourmaline support ensure even adsorption and nucleation of MoS<sub>2</sub> species through promoting the thermal vibration and reducing the diffusion activation energy of Mo and S atoms. Meanwhile, strong electric field on the surface of tourmaline can restrain the recombination of photo-generated electron–hole pairs (Tzeng et al. 2019). This work provides an inspiring scheme for low-cost batch preparation of high-quality two-dimensional materials via assembly on tourmaline mineral functional materials.

## Materials and methods

### Materials

The tourmaline was provided by HY Technology Co., Ltd. The ammonium molybdate (NH<sub>4</sub>)<sub>6</sub>Mo<sub>7</sub>O<sub>24</sub>·4H<sub>2</sub>O, thiourea (CH<sub>4</sub>N<sub>2</sub>S) and rhodamine B (RhB) were supplied by Kewei Chemical Group Co., Ltd. These materials were used as received. Deionized (DI) water was used in all experiments.

### Synthesis of MoS<sub>2</sub>/tourmaline composites

2.4 g (NH<sub>4</sub>)<sub>6</sub>Mo<sub>7</sub>O<sub>24</sub>·4H<sub>2</sub>O and 2.28 g CH<sub>4</sub>N<sub>2</sub>S were dissolved in 70 mL deionized water and stirred for 0.5 h. Then, 0.84 g of tourmaline powder was added into the above solution and mechanically stirred for another 0.5 h. Next, the suspension was sonicated for 0.5 h. After that, 50 mL of the above suspension was transferred into a 100 mL Teflon-lined stainless steel autoclave and kept at different hydrothermal temperatures including 190, 200, 210, 220, and 230 °C for 3 h. After the samples were cooled to room temperature, the final products were obtained by filtration, washed thoroughly with deionized water, and dried at 80 °C for 12 h. The samples synthesized at 190 °C, 200 °C, 210 °C, 220 °C, and 230 °C were named as T-190, T-200, T-210, T-220, and T-230, respectively.

### Characterizations

X-ray diffraction was performed on a D8 ADVANCE X-ray diffractometer with nickel-filtered Cu K $\alpha$  radiation as the X-ray source, and  $V = 40$  kV,  $I = 40$  mA, and  $\lambda = 1.54$  Å. Fourier-transform infrared spectroscopy (FTIR) spectra were recorded in transmission mode from 400 to 4000 cm<sup>-1</sup> on a Tensor II Fourier transform infrared spectrometer purchased

from Bruker in Germany. The morphology of the samples was observed using a Quanta FEG450 scanning electron microscope working at 200 kV. Transmission electron microscope (TEM) and high-resolution TEM (HRTEM) images were acquired using a JEM 2100F transmission electron microscope from JEOL in Japan at an accelerating voltage of 200 kV. X-ray photoelectron spectroscopy (XPS) measurements were performed on an ESCALAB250 spectrometer.

The atomic resolution scanning transmission electron microscope (STEM) was realized on a JEM-ARM200F equipped with EDS analyzer (200 kV, probe Cs-corrector, 68–174 mrad collection angle for high-angle annular dark field imaging,  $\sim 0.8$  Å spatial resolution). The samples were ground into fine powders, dispersed in ethanol, dropped onto a lacey carbon film-Cu TEM ready grid from Ted-Pella Co., and then dried on a hot plate at 70 °C. STEM images were taken using the high-angle annular dark field detector. Energy-dispersive X-ray spectroscopy (EDS) was measured on an EDS analyzer (JEOL, EX-230 100 m<sup>2</sup> detector) equipped on a JEM-ARM200F microscope. The elemental mapping was performed at a sampling resolution of 128 × 128 pixels and a dwell time of 0.1 ms/pixel under multiple frame integration.

### Computational methodology

Density functional theory (DFT) calculations were conducted using the Vienna Ab-initio Simulation Package (VASP). The core and valence electrons were described by the projector augmented wave method (Blöchl 1994) and the Kohn–Sham wave functions being expanded in plane wave basis (Kohn and Sham 1965). The energy cutoff was set as 400 eV for all of the calculations. The electronic exchange and correlation were described by a generalized gradient approximation; the functional method developed by Perdew, Burke, and Ernzerhof was chosen for the calculations (Perdew et al. 1996). The Brillouin zone was sampled within a (3 × 3 × 1) *k*-point mesh using the method developed by Monkhorst and Pack (Monkhorst and Pack 1976). Structures were considered as being optimized after all the forces fell below 0.05 eV per Å.

### Photocatalytic tests

Photocatalytic activity of the as-prepared samples was assessed by the photocatalytic degradation of rhodamine B under visible light irradiation, where optical absorption of rhodamine B at 553 nm was used as a major wavelength. In a typical experiment, 20 mg of sample was added into 100 mL of rhodamine B solution, yielding the suspension under stirring in the dark for 0.5 h to reach the adsorption/desorption equilibrium. The suspension was subjected to irradiation by

a 500 W Xe lamp at  $\lambda > 420$  nm under stirring at ambient conditions. At intervals of 0.5 h, 6 mL of the suspension was extracted and centrifuged to remove the photocatalysts. The filtrates were analyzed by recording the UV–vis spectra using a Shimadzu UV-1800 spectrophotometer (Osman et al. 2017). The residual percentage of the rhodamine B is calculated through  $C_t/C_0$ , where  $C_0$  represents the concentration of rhodamine B before the irradiation,  $C_t$  represents the concentration of rhodamine B after irradiating time *t* was utilized to represent the photocatalytic performance of the catalyst.

## Results and discussion

Here we studied the phase, morphology, structure, vibrational bands and the specific interactions, surface elemental composition and chemical status of the as-prepared MoS<sub>2</sub>/tourmaline composites, and the growth mechanism of the composite was raised. Next, the photocatalytic test was carried out and both density functional theory calculations and proposed synergic effects between tourmaline and MoS<sub>2</sub> for rhodamine B degradation were used to explain the high catalytic efficiency of the composite.

### Morphology observation of the MoS<sub>2</sub>/tourmaline composite

Scanning electron microscopy images of the as-prepared MoS<sub>2</sub>/tourmaline composites delineate the overall architectures. For the MoS<sub>2</sub>/tourmaline samples, MoS<sub>2</sub> nanosheets are evenly distributed on the surface of tourmaline particles, displaying a gripping pangolin-like structure (Fig. 1a and Fig. S1). As the synthesis temperature ramps, the coverage of the MoS<sub>2</sub> nanosheets over the tourmaline particles increases. As revealed by Fig. 1a, MoS<sub>2</sub> nanosheets are consistently grown on the surface of tourmaline particles in the sample prepared at 210 °C. High-resolution transmission electron microscope image (Fig. S2) further shows direct evidence that MoS<sub>2</sub> phase has been uniformly loaded on the tourmaline particles, which benefits charge separation during electron transfer (Yin et al. 2017) and catalytic efficiency.

### Phase study of the MoS<sub>2</sub>/tourmaline composite

X-ray diffraction patterns further testified the phases compositions of tourmaline (JCPDS Card No. 43–1464) and 2H-MoS<sub>2</sub> (JCPDS Card No.37–1492). As shown in Fig. 1c, the peak of the MoS<sub>2</sub> diffraction (002) shifts slightly to a smaller angle, which is probably due to the inhalation of ammonium ions into the MoS<sub>2</sub> layers (Wang et al. 2020). Meanwhile, the specific peaks of the tourmaline diffraction

shift to larger angles indicating the shrinkage of tourmaline unit cell (Table S1), which is caused by the oxidation of  $\text{Fe}^{2+}$  to  $\text{Fe}^{3+}$  inside the tourmaline. (Guo 2019). The diffraction peak becomes sharper as the temperature increases, indicating the crystallinity of  $\text{MoS}_2$  is enhanced (Wang et al. 2014), and the various fabrication times demonstrate a consistent tendency with the temperature change (Figs. S3, S4).

### FTIR and X-ray spectroscopy analysis of the $\text{MoS}_2$ /tourmaline composite

FTIR results (Fig. 1d) identified the functional groups of the tourmaline skeleton, such as the stretching vibration at  $3562\text{ cm}^{-1}$  for O–H,  $1266\text{ cm}^{-1}$  and  $1350\text{ cm}^{-1}$  for antisymmetric B–O,  $980\text{ cm}^{-1}$  for Si–O–Al,  $712\text{ cm}^{-1}$ ,  $780\text{ cm}^{-1}$  and  $1030\text{ cm}^{-1}$  for Si–O–Si,  $491\text{ cm}^{-1}$ ,  $573\text{ cm}^{-1}$ , and  $655\text{ cm}^{-1}$  for octahedral cation M–O, along with the  $470\text{ cm}^{-1}$  for Mo–S stretching vibration (Luo et al. 2020; Yu et al. 2020; Pramoda et al. 2016). Furthermore, XPS measurements show a significant overall blue shift for  $\text{MoS}_2$  when assembling on the tourmaline (Fig. S5), indicating the fact of

electron transfer from  $\text{MoS}_2$  to the tourmaline support with the surface electric field (Liu et al. 2015a).

### Atomic structural details for tourmaline, $\text{MoS}_2$ and their interface

To study the atomic structures of the synthesized  $\text{MoS}_2$ /tourmaline composites, probe aberration-corrected scanning transmission electron microscopy (AC-STEM) was performed (Fig. 2). High-angle annular dark field imaging combined with X-ray EDS was also used to further characterize the morphology of  $\text{MoS}_2$ /tourmaline composite (Fig. 2a), atomic structure details of tourmaline (Fig. 2b, c), and  $\text{MoS}_2$ -tourmaline interface (Fig. 2d). It can be seen that tourmaline structures facilitate a good dispersion of the two-dimensional  $\text{MoS}_2$  nanosheets (Figs. 1b, 2a). Particularly, this turns to be the first time to directly image the atomic structure of a tourmaline crystal (Fig. 2b), where the atom-coordination details are in good agreement with the ideal structure (Bosi et al. 2005). It proves that tourmaline belongs to the  $R_{3m}$  space group with six-membered Si rings, Fe–Mg

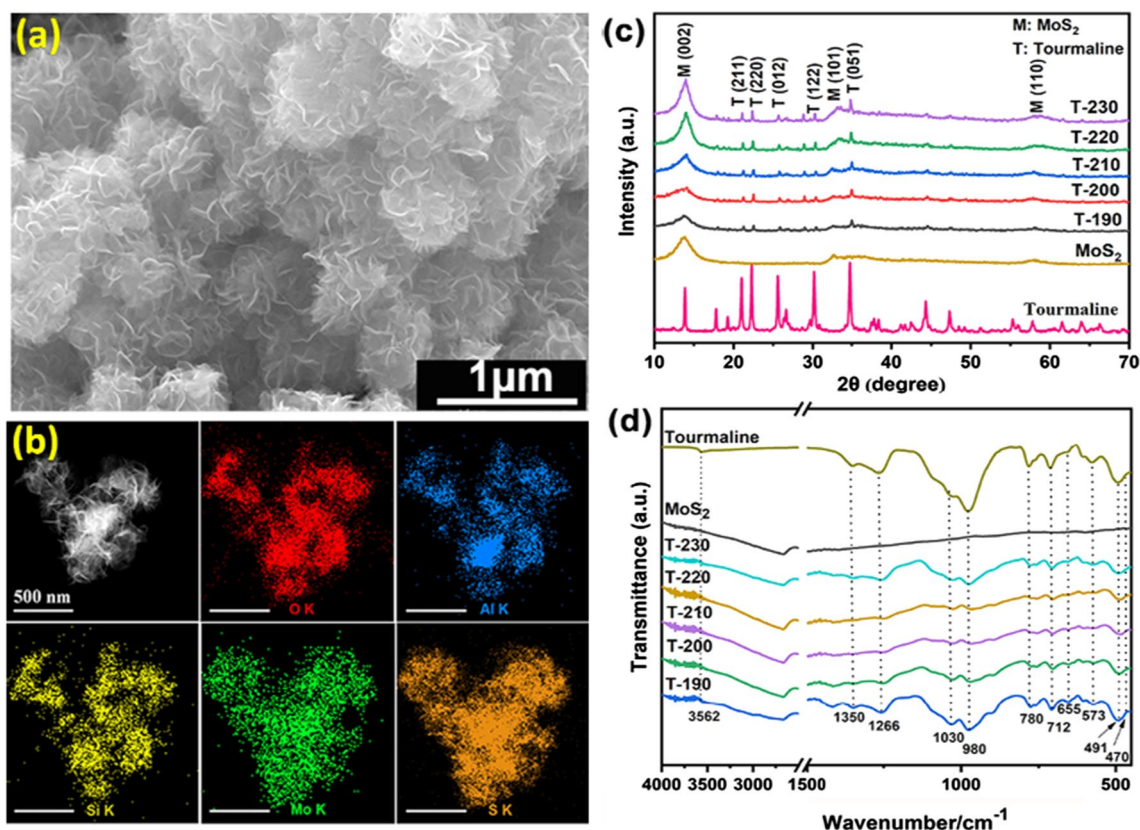


**Fig. 1** Morphology and phase composition of the as-fabricated  $\text{MoS}_2$ /tourmaline composites. **a** Scanning electron microscopy images of the  $\text{MoS}_2$ /tourmaline composite obtained via microwave hydrothermal at 210  $^{\circ}\text{C}$ ; **b** Energy-dispersive X-ray spectroscopy (EDS) mappings for elemental distributions of the individual  $\text{MoS}_2$ /tourmaline

structure; **c** X-ray diffraction patterns of the as-prepared samples synthesized at various temperatures; **d** Fourier-transform infrared (FTIR) analysis of functional groups on the surface of as-fabricated samples, where T-190, T-200, T-210, T-220, T-230 correspond to the sample prepared at 190  $^{\circ}\text{C}$ , 200  $^{\circ}\text{C}$ , 210  $^{\circ}\text{C}$ , 220  $^{\circ}\text{C}$ , 230  $^{\circ}\text{C}$ , respectively

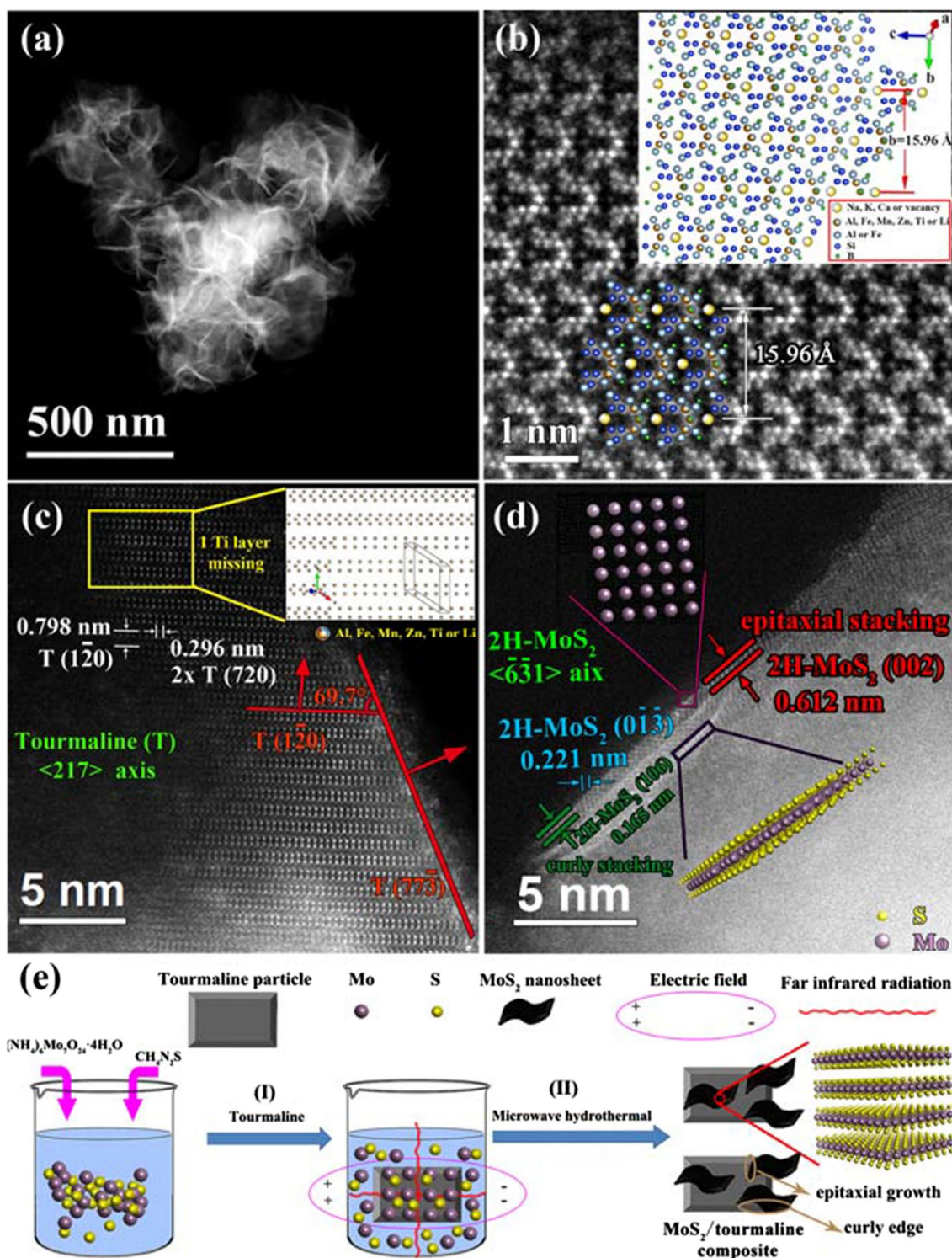


**Fig. 2** Scanning transmission electron microscopy (STEM) analysis on the atomic structure of MoS<sub>2</sub>/tourmaline (T-210) composite, where T represents tourmaline. **a** A low-magnified STEM image shows two-dimensional MoS<sub>2</sub> nanosheets assembled along the tourmaline surface; **b** Enlarged high-angle annular dark field images: the

atomic structure details of tourmaline, the further details observed by tourmaline <217> axis (**c**) and MoS<sub>2</sub>-tourmaline interface (**d**); **e** Growth mechanism of MoS<sub>2</sub>/tourmaline composites. I: Even distribution and adsorption process of Mo and S atoms and clusters on the tourmaline surface; II: Microwave hydrothermal synthesis process

octahedra, B triangles; structural units linked together by Al octahedra (Bosi and Lucchesi 2007). This unique structure is noncentrosymmetric and polar, the *c* axis is threefold symmetry, and there is no axis plane of symmetry perpendicular to *c* and no center of symmetry (Nakamura et al. 1992; Wang et al. 2011). Therefore, tourmaline is usually in the shapes of trilateral and hexagonal column, with properties of far infrared radiation, spontaneous polarization, pyroelectricity, and piezoelectricity (Wang et al. 2019; Chen et al. 2020; Dietrich 1985). Moreover, close examination of tourmaline/MoS<sub>2</sub> interface reveals it was the uniform anchor of MoS<sub>x</sub> clusters on the mineral surface of tourmaline (77 $\bar{3}$ ) facets (Fig. 2c) that benefits the uniform growth of MoS<sub>2</sub> nanosheets, while these MoS<sub>2</sub> sheets are in atomic thickness of only 3–4 layers epitaxially stacking (Zhang et al. 2017b) in a 2H sequence on the mineral surface in relationship of tourmaline (77 $\bar{3}$ )||MoS<sub>2</sub> (002) (Fig. 2d). Intriguingly, the MoS<sub>2</sub> nanosheets evolve into curly and intercross morphology, which according to the microscopy evidence, herein, should be attributed to the intrinsic behaviors of MoS<sub>2</sub> layer rolling up during

stacking at the tourmaline/MoS<sub>2</sub> interface, e.g., in Fig. 2d, the initial MoS<sub>2</sub>(002) termination rolls up to be MoS<sub>2</sub>(106).

### Proposed growth mechanism of MoS<sub>2</sub>/tourmaline composite

According to the above structural analysis, the growth mechanism of MoS<sub>2</sub>/tourmaline composites can be illustrated schematically in Fig. 2e, where Mo and S atoms gradually adhere to the tourmaline followed by the epitaxial growth of MoS<sub>2</sub> nanosheets with curly edges on the surface of tourmaline particles. More surprisingly, using the naturally abundant mineral to support highly dispersed MoS<sub>2</sub>, the fabrication cost has been reduced to be less than one-thousandth of the commercial counterparts (Fig. S6).

### Density functional theory calculations

To understand the potential structure–activity relation of MoS<sub>2</sub>/tourmaline, DFT calculations were performed to study the bandgap and *d*-band center, i.e., average energy of *d*-electrons of MoS<sub>2</sub> with the number of layer varying from 1 to 4 (Fig. 3).

Interestingly, it can be seen that reducing the thickness leads to a wider bandgap (Fig. 3a), while a monolayer of MoS<sub>2</sub> owns the bandgap close to that of optimum for photocatalysis (Liu et al. 2015b). Meanwhile, with a thinner layer of MoS<sub>2</sub>, there is a significant upshift of the *d*-band center toward the Fermi level, indicating stronger bond activation capacity for degradation reaction (Li et al 2019). Both these theoretical calculations indicate a significant advantage of using tourmaline for the preparation of MoS<sub>2</sub>: The use of tourmaline results in a controllable thickness of MoS<sub>2</sub>, while a thin layer of MoS<sub>2</sub> guarantees a better photocatalytic activity.

### Photocatalytic performance of the composite toward rhodamine B degradation

Photocatalysis is an effective technology which has been frequently utilized for water splitting and degradation of organic pollutants (Li et al. 2020; Liao et al. 2019; Zhong et al. 2018). The photocatalytic activity of the MoS<sub>2</sub>/tourmaline composites was evaluated using the rhodamine B degradation as a probe reaction, as shown in Fig. 4. The degradation processes of all the MoS<sub>2</sub>/tourmaline composites exhibit much higher efficiencies than that, ~41.2%, of the pure MoS<sub>2</sub> after photocatalytic reaction for 150 min (Fig. 4a). Notably, the T-210 sample reaches the highest degradation efficiency of ~93%, roughly 2.3 times the degradation efficiency of the pure MoS<sub>2</sub>. These numbers suggest that the distinct architecture of the MoS<sub>2</sub>/tourmaline composite produces much greater photocatalytic degradation efficiency. In addition, the

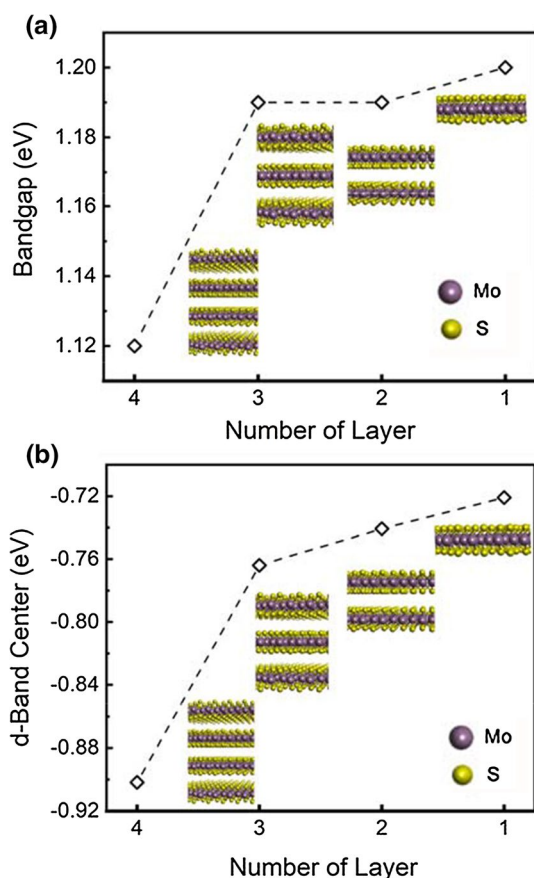
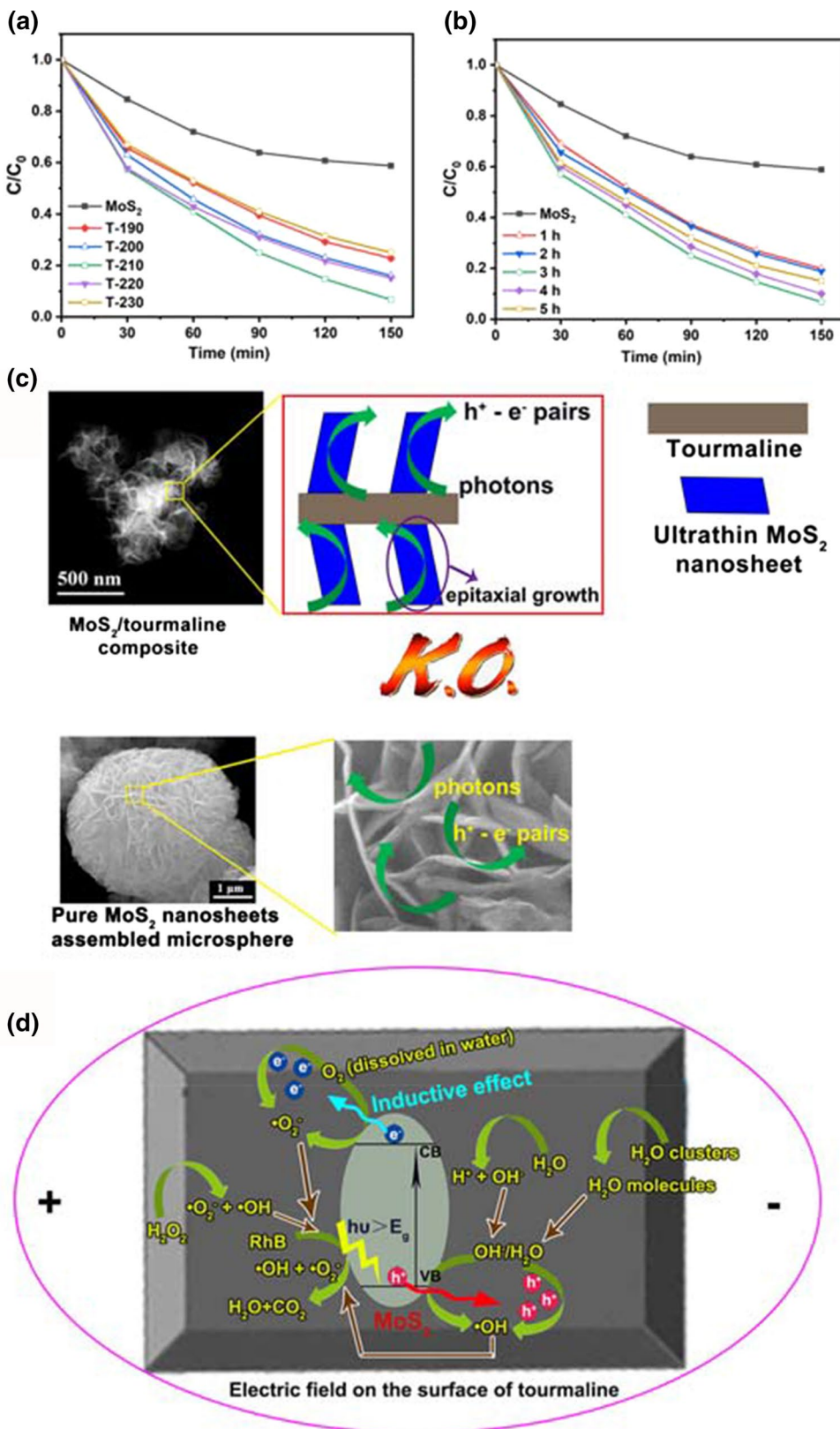


**Fig. 3** Note the increase in the calculated bandgap (a) and *d*-band center (b) of MoS<sub>2</sub> with the number of layer varying from 4 to 1. Insets show the optimized structures considered for calculations

**Fig. 4** Photocatalytic performance and mechanism of rhodamine B degradation. Photocatalytic activity of the MoS<sub>2</sub>/tourmaline composites prepared at different temperatures (a) and times (b). It is worth noting the sample prepared at 210 °C and 3 h exhibits higher photocatalytic activity than those prepared at other synthetic parameters and much higher than pure MoS<sub>2</sub>, where T-190, T-200, T-210, T-220, T-230 correspond to the sample prepared at 190 °C, 200 °C, 210 °C, 220 °C, 230 °C, respectively; c Comparison of the photocatalytic sites between MoS<sub>2</sub>/tourmaline composite and pure MoS<sub>2</sub> microsphere; d Illustration of the reaction steps involved in the MoS<sub>2</sub>/tourmaline composite, in which the synergic effects between tourmaline and MoS<sub>2</sub> are worthy of paying attention especially



T-220 and T-230 samples exhibit a slightly lower degradation rate than the T-210, which may be due to the agglomeration of MoS<sub>2</sub> nanosheets at higher temperature. For all the samples, the changes in the fabrication time (Fig. 4a) and fabrication temperature (Fig. 4b) exhibit similar tendencies.

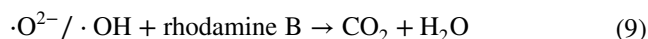
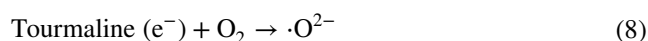
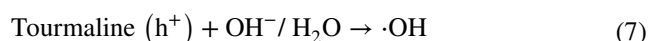
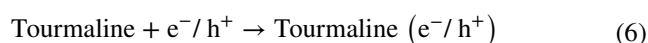
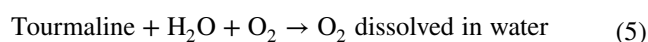
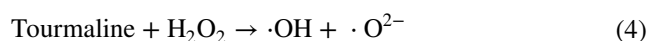
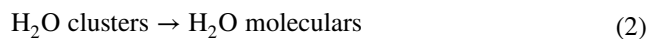
### Comparison of pristine MoS<sub>2</sub> and MoS<sub>2</sub>/tourmaline composite during photocatalysis

Evidently, although the as-synthesized MoS<sub>2</sub> microspheres are assembled by MoS<sub>2</sub> nanosheets (Fig. 4c), most of them are encapsulated inside of the microspheres, which have little-to-zero access to the visible light irradiation and thus contribute much less to the photocatalytic degradation of rhodamine B compared with the outmost MoS<sub>2</sub> nanosheets in the microspheres. In contrast, MoS<sub>2</sub> nanosheets in the MoS<sub>2</sub>/tourmaline composite are highly dispersed, offering much more exposed 3–4 layered ultrathin MoS<sub>2</sub> nanosheets with the epitaxial and curly stacking for the photocatalysis process, which enhanced the absorption of photons and the efficiency of charge transfer (Fig. 4c) (Zhou et al. 2019; Dai et al. 2016).

### Proposed synergic effects between tourmaline and MoS<sub>2</sub> in photocatalytic rhodamine B degradation

Figure 4d further illustrates the synergic effects between the tourmaline and the grown MoS<sub>2</sub> nanosheets in the MoS<sub>2</sub>/tourmaline composite. First, OH is the dominant oxidant for photocatalytic degradation in wastewater treatment, tourmaline can polarize water (Wang et al. 2012) to produce OH<sup>-</sup> (Eq. 1) and decrease the water association degree on the tourmaline surface (Eq. 2) (Tzeng et al. 2019), thus it can form more •OH species from the oxidation of OH<sup>-</sup> or H<sub>2</sub>O via photogenerated holes (Eq. 3). Second, tourmaline, schorl herein, is a natural mineral bearing iron ions, which can catalyze H<sub>2</sub>O<sub>2</sub> that formed in the photocatalytic reaction to produce •OH and •O<sup>2-</sup> (Eq. 4) (Xu et al. 2010; Wang et al. 2013), the details of the formation of H<sub>2</sub>O<sub>2</sub>, as well as its catalytic mechanism, are shown in Fig. S7. Third, the holes show high affinities for the electrons and the high degree of the recombination of the electron–hole pairs is a major limiting factor controlling the photocatalytic efficiency. O<sub>2</sub> acts primarily as an efficient electron trap to prevent the recombination of the photogenerated electron–hole pairs, while tourmaline can augment the content of dissolved O<sub>2</sub> in water by ionizing water (Eq. 5) (Wang et al. 2013). Fourth, the photo-induced electrons from the MoS<sub>2</sub> are adsorbed tightly on the anode of tourmaline due to the ‘electrostatic poles’ on the surface of tourmaline, which prolongs the charge lifetime from MoS<sub>2</sub> (Eq. 6) (Yu et al. 2016). Such retardation effect of charge not only results in trapping the charge to suppress

the recombination of h<sup>+</sup>–e<sup>-</sup> pairs, but also transferring the trapped charges to contact with the reactants (Eq. 7). In the mean time, the remaining holes also migrate outward to form reactive species (Eq. 8). Therefore, the MoS<sub>2</sub>/tourmaline composite demonstrates much higher photocatalytic activity than that of the pure MoS<sub>2</sub> microspheres (Eq. 9). The main steps of the synergic effects are shown as follows:



In conclusion, the unique MoS<sub>2</sub>/tourmaline structure with the excellent synergism of tourmaline significantly facilitates photocatalytic degradation compared with the pure MoS<sub>2</sub> microspheres.

## Conclusion

MoS<sub>2</sub> nanosheets with 3–4 atomic layers are uniformly assembled on the tourmaline particles via a facile microwave hydrothermal method. In this new composite architecture, tourmaline carrier is in a form of polyhedron single crystal which supports the epitaxial growth of 2H-MoS<sub>2</sub> layers at the tourmaline (773) facets, while an intrinsic rolling up behavior of MoS<sub>2</sub> layer along the support surface from direction [002] to [106] accounts for the structural origin of the overall curly morphology. In a typical photocatalytic application, the as-prepared MoS<sub>2</sub>/tourmaline has demonstrated considerably enhanced photocatalytic rhodamine B degradation. To the best of our knowledge, this is the first report on the combination of atomically thin two-dimensional MoS<sub>2</sub> nanosheets and tourmaline mineral. Density functional theory calculations further showed that thinner MoS<sub>2</sub> nanosheets lead



to wider bandgap and the upshift of *d*-band centers, which in turn enhances the photocatalytic activity. This work provides new insights for the low-cost mass production of high-quality, atomically thin two-dimensional materials supported on tourmaline minerals.

**Supplementary Information** The online version contains supplementary material available at <https://doi.org/10.1007/s10311-021-01235-6>.

**Acknowledgements** This work was financially supported by the National Natural Science Foundation of China (No. 51874115), the Postdoctoral Science Foundation funded project of China (No. 2020T130166), the CAS Youth Innovation Promotion Association (No. 2019190), the Introduced Overseas Scholars Program of Hebei province, China (No. C201808), the Enterprise Science and Technology Commissioner Project of Tianjin City, China (No. 19JCTPJC56100) and the Excellent Young Scientist Foundation of Hebei province, China (No. E2018202241).

**Authors' contribution** FW and JL conceived and supervised experiments. MH, LC, XX and DW performed experiments. WL and FW performed and analyzed the STEM characterization. HL performed the DFT simulations. FW, WL, BF, MH and LC prepared and revised the manuscript. All authors contributed to the experiments and manuscript preparation.

**Data availability** The data that support the findings of this study are available from the corresponding author upon reasonable request.

## Declarations

**Conflict of interests** The authors declared that they have no conflict of interest.

## References

- Blöchl PE (1994) Projector augmented-wave method. *Phys Rev B* 50:17953–17979. <https://doi.org/10.1103/PhysRevB.50.17953>
- Bosi F, Lucchesi S (2007) Crystal chemical relationships in the tourmaline group: structural constraints on chemical variability. *Am Miner* 92:1054–1063. <https://doi.org/10.2138/am.2007.2370>
- Bosi F, Andreozzi GB, Federico M et al (2005) Crystal chemistry of the elbaite-schorl series. *Am Miner* 90:1784–1792. <https://doi.org/10.2138/am.2005.1827>
- Chen Q, Wang C, Qiao Z et al (2020) Graphene/tourmaline composites as a filler of hot mix asphalt mixture: preparation and properties. *Constr Build Mater* 239:117859. <https://doi.org/10.1016/j.conbuildmat.2019.117859>
- Dai R, Zhang A, Pan Z et al (2016) Epitaxial growth of lattice-mismatched core-shell TiO<sub>2</sub>@MoS<sub>2</sub> for enhanced lithium-ion storage. *Small* 12:2792–2799. <https://doi.org/10.1002/sml.20160237>
- de Lima BRM, do Nascimento NMP, Zamian JR et al (2020) Higher dye degradation using a visible-light photocatalyst made of mesoporous graphitic carbon nitride prepared with the Tween-40 surfactant. *Environ Chem Lett* 18:1413–1422. <https://doi.org/10.1007/s10311-020-01008-7>
- Dietrich R (1985) *The tourmaline group*. Springer, Boston
- Gan X, Lei D, Ye R et al (2020) Transition metal dichalcogenide-based mixed-dimensional heterostructures for visible-light-driven photocatalysis: dimensionality and interface engineering. *Nano Res* 14:2003–2022. <https://doi.org/10.1007/s12274-020-2955-x>
- Guerra DL, Oliveira SP, Silva EM, Batista AC (2012) Adsorption of uranyl on beryl and tourmaline; kinetics and thermodynamic investigation. *Int J Miner Process* 102:25–31. <https://doi.org/10.1016/j.minpro.2011.09.007>
- Guo B (2019) Effect of oxygen storage/transport capacity of nano-Ce<sub>1-x</sub>Zr<sub>x</sub>O<sub>2</sub> on far-infrared emission property of natural tourmaline. *J Alloy Compd* 785:1121–1125. <https://doi.org/10.1016/j.jallcom.2019.01.238>
- Hao M, Gao P, Liu W et al (2021) Microwave hydrothermal-reduction synthesis of zanthoxylum trunk-like Co/CoAl<sub>2</sub>O<sub>4</sub>/sepiolite nanocomposite. *Ceram Int* 47:4722–4728. <https://doi.org/10.1016/j.ceramint.2020.10.041>
- Kohn W, Sham LJ (1965) Self-consistent equations including exchange and correlation effects. *Phys Rev* 140:A1133–A1138. <https://doi.org/10.1103/PhysRev.140.A1133>
- Kumar R, Sahoo S, Joanni E et al (2019) A review on synthesis of graphene, h-BN and MoS<sub>2</sub> for energy storage applications: recent progress and perspectives. *Nano Res* 12:2655–2694. <https://doi.org/10.1007/s12274-019-2467-8>
- Li G, Chen D, Zhao W et al (2015) Efficient adsorption behavior of phosphate on La-modified tourmaline. *J Environ Chem Eng* 3:515–522. <https://doi.org/10.1016/j.jece.2015.01.010>
- Li Z, Meng X, Zhang Z (2018) Few-layer MoS<sub>2</sub> nanosheets-deposited on Bi<sub>2</sub>MoO<sub>6</sub> microspheres: a Z-scheme visible-light photocatalyst with enhanced activity. *Catal Today* 315:67–78. <https://doi.org/10.1016/j.cattod.2018.03.014>
- Li H, Chai W, Henkelman G (2019) Selectivity for ethanol partial oxidation: the unique chemistry of single-atom alloy catalysts on Au, Ag, and Cu (111). *J Mater Chem A* 7:23868–23877. <https://doi.org/10.1039/C9TA04572D>
- Li S, Ruan L, Wang S et al (2020) Surface energy-driven solution epitaxial growth of anatase TiO<sub>2</sub> homostructures for overall water splitting. *J Mater Sci Technol* 46:139–144. <https://doi.org/10.1016/j.jmst.2020.01.038>
- Liao G, Gong Y, Zhang L et al (2019) Semiconductor polymeric graphitic carbon nitride photocatalysts: the “holy grail” for the photocatalytic hydrogen evolution reaction under visible light. *Energy Environ Sci* 12:2080–2147. <https://doi.org/10.1039/C9EE00717B>
- Liu N, Guo Y, Yang X et al (2015a) Microwave-assisted reactant-protecting strategy toward efficient MoS<sub>2</sub> electrocatalysts in hydrogen evolution reaction. *ACS Appl Mater Interfaces* 7:23741–23749. <https://doi.org/10.1021/acsami.5b08103>
- Liu C, Wang L, Tang Y et al (2015b) Vertical single or few-layer MoS<sub>2</sub> nanosheets rooting into TiO<sub>2</sub> nanofibers for highly efficient photocatalytic hydrogen evolution. *Appl Catal B* 164:1–9. <https://doi.org/10.1016/j.conbuildmat.2019.117859>
- Liu Y, Xu X, Zhang H et al (2018) Flower-like MoS<sub>2</sub> on graphitic carbon nitride for enhanced photocatalytic and electrochemical hydrogen evolutions. *Appl Catal B* 239:334–344. <https://doi.org/10.1016/j.apcatb.2018.08.028>
- Luo G, Chen A, Zhu M et al (2020) Improving the electrocatalytic performance of Pd for formic acid electrooxidation by introducing tourmaline. *Electrochim Acta* 360:137023. <https://doi.org/10.1016/j.electacta.2020.137023>
- Madima N, Mishra SB, Inamuddin I et al (2020) Carbon-based nanomaterials for remediation of organic and inorganic pollutants from wastewater. A review. *Environ Chem Lett* 18:1169–1191. <https://doi.org/10.1007/s10311-020-01001-0>
- Mecha AC, Chollom MN (2020) Photocatalytic ozonation of wastewater: a review. *Environ Chem Lett* 18:1491–1507. <https://doi.org/10.1007/s10311-020-01020-x>

- Monkhorst HJ, Pack JD (1976) Special points for Brillouin-zone integrations. *Phys Rev B* 13:5188–5192. <https://doi.org/10.1103/PhysRevB.13.5188>
- Nakamura T, Kubo T (1992) Tourmaline group crystals reaction with water. *Ferroelectrics* 137:13–31. <https://doi.org/10.1080/00150199208015933>
- Osman H, Su Z, Ma X (2017) Efficient photocatalytic degradation of rhodamine B dye using ZnO/graphitic C<sub>3</sub>N<sub>4</sub> nanocomposites synthesized by microwave. *Environ Chem Lett* 15:435–441. <https://doi.org/10.1007/s10311-017-0604-8>
- Perdew JP, Burke K, Ernzerhof M (1996) Generalized gradient approximation made simple. *Phys Rev Lett* 77:3865–3868. <https://doi.org/10.1103/PhysRevLett.77.3865>
- Pramoda K, Gupta U, Ahmad I et al (2016) Assemblies of covalently cross-linked nanosheets of MoS<sub>2</sub> and of MoS<sub>2</sub>-RGO: synthesis and novel properties. *J Mater Chem A* 4:8989–8994. <https://doi.org/10.1039/C6TA00645K>
- Qu Y, Duan X (2013) Progress, challenge and perspective of heterogeneous photocatalysts. *Chem Soc Rev* 42:2568–2580. <https://doi.org/10.1039/C2CS35355E>
- Saeed M, Ahmad A, Boddula R et al (2018) Ag@Mn<sub>x</sub>O<sub>y</sub>: an effective catalyst for photo-degradation of rhodamine B dye. *Environ Chem Lett* 16:287–294. <https://doi.org/10.1007/s10311-017-0661-z>
- Saja S, Bouazizi A, Achiou B et al (2020) Fabrication of low-cost ceramic ultrafiltration membrane made from bentonite clay and its application for soluble dyes removal. *J Eur Ceram Soc* 40:2453–2462. <https://doi.org/10.1016/j.jeurceramsoc.2020.01.057>
- Saravanan A, Kumar PS, Vo DVN et al (2021) Photocatalysis for removal of environmental pollutants and fuel production: a review. *Environ Chem Lett* 19:441–463. <https://doi.org/10.1007/s10311-020-01077-8>
- Sun Y, Alimohammadi F, Zhang D, Guo G (2017) Enabling colloidal synthesis of edge-oriented MoS<sub>2</sub> with expanded interlayer spacing for enhanced HER catalysis. *Nano Lett* 17:1963–1969. <https://doi.org/10.1021/acs.nanolett.6b05346>
- Tzeng JH, Weng CH, Lin YH et al (2019) Synthesis, characterization, and visible light induced photoactivity of tourmaline-N-TiO<sub>2</sub> composite for photooxidation of ethylene. *J Ind Eng Chem* 80:376–384. <https://doi.org/10.1016/j.jiec.2019.08.017>
- Wang Z, Mi B (2017) Environmental applications of 2D molybdenum disulfide (MoS<sub>2</sub>) nanosheets. *Environ Sci Technol* 51:8229–8244. <https://doi.org/10.1021/acs.est.7b01466>
- Wang C, Wu J, Sun H et al (2011) Adsorption of Pb(II) ion from aqueous solutions by tourmaline as a novel adsorbent. *Ind Eng Chem Res* 50:8515–8523. <https://doi.org/10.1021/ie102520w>
- Wang C, Liu J, Zhang Z et al (2012) Adsorption of Cd (II), Ni (II), and Zn (II) by tourmaline at acidic conditions: kinetics, thermodynamics, and mechanisms. *Ind Eng Chem Res* 51:4397–4406. <https://doi.org/10.1021/ie2023096>
- Wang C, Zhang Y, Yu L et al (2013) Oxidative degradation of azo dyes using tourmaline. *J Hazard Mater* 260:851–859. <https://doi.org/10.1016/j.jhazmat.2013.06.054>
- Wang Q, Yun G, Bai Y et al (2014) Photodegradation of rhodamine B with MoS<sub>2</sub>/Bi<sub>2</sub>O<sub>3</sub>/CO<sub>2</sub> composites under UV light irradiation. *Appl Surf Sci* 313:537–544. <https://doi.org/10.1016/j.apsusc.2014.06.018>
- Wang F, Zhang H, Liang J et al (2017) Effect of tourmaline addition on the structure of silica hollow microspheres prepared by a novel template method. *J Alloy Compd* 693:1323–1327. <https://doi.org/10.1016/j.jallcom.2016.09.141>
- Wang F, Xie Z, Liang J et al (2019) Tourmaline-modified FeMnTiO<sub>x</sub> catalysts for improved low-temperature NH<sub>3</sub>-SCR performance. *Environ Sci Technol* 53:6989–6996. <https://doi.org/10.1021/acs.est.9b02620>
- Wang F, Hao M, Liu W et al (2020) Low-cost fabrication of highly dispersed atomically-thin MoS<sub>2</sub> nanosheets with abundant active Mo-terminated edges. *Nano Mater Sci*. <https://doi.org/10.1016/j.nanoms.2020.10.007>
- Wang F, Ding Y, Hao M et al (2021) Novel fabrication of a sepiolite supported cobalt-based catalyst via a coprecipitation-reduction method. *Appl Clay Sci* 200:105909. <https://doi.org/10.1016/j.clay.2020.105909>
- Xu H, Zheng Z, Mao G (2010) Enhanced photocatalytic discoloration of acid fuchsine wastewater by TiO<sub>2</sub>/schorl composite catalyst. *J Hazard Mater* 175:658–665. <https://doi.org/10.1016/j.jhazmat.2009.10.059>
- Xu J, Liu X, Lowry GV et al (2016) Dechlorination mechanism of 2,4-dichlorophenol by magnetic MWCNTs supported Pd/Fe nanohybrids: rapid adsorption, gradual dechlorination, and desorption of phenol. *ACS Appl Mater Interfaces* 11:7333–7342. <https://doi.org/10.1021/acsami.5b11859>
- Xu J, Cao Z, Wang Y et al (2019) Distributing sulfidized nanoscale zerovalent iron onto phosphorus-functionalized biochar for enhanced removal of antibiotic florfenicol. *Chem Eng J* 359:713–722. <https://doi.org/10.1016/j.cej.2018.11.180>
- Xu J, Liu X, Cao Z et al (2020) Fast degradation, large capacity, and high electron efficiency of chloramphenicol removal by different carbon-supported nanoscale zerovalent iron. *J Hazard Mater* 384:121253. <https://doi.org/10.1016/j.jhazmat.2019.121253>
- Yin L, Zhao M, Hu H et al (2017) Synthesis of graphene/tourmaline/TiO<sub>2</sub> composites with enhanced activity for photocatalytic degradation of 2-propanol. *Chin J Catal* 38:1307–1314. [https://doi.org/10.1016/S1872-2067\(17\)62795-5](https://doi.org/10.1016/S1872-2067(17)62795-5)
- Yu L, Wang C, Chen F et al (2016) Investigating the synergistic effects in tourmaline/TiO<sub>2</sub>-based heterogeneous photocatalysis: underlying mechanism insights. *J Mol Catal A Chem* 411:1–8. <https://doi.org/10.1016/j.molcata.2015.10.006>
- Yu C, Wen M, Tong Z et al (2020) Synthesis and enhanced photocatalytic performance of 0D/2D CuO/tourmaline composite photocatalysts. *Beilstein J Nanotechnol* 11:407–416. <https://doi.org/10.3762/bjnano.11.31>
- Zhang H, Zhang R, Zhang G et al (2014) Modified graphite electrode by polyaniline/tourmaline improves the performance of bio-cathode microbial fuel cell. *Int J Hydrogen Energy* 39:11250–11257. <https://doi.org/10.1016/j.ijhydene.2014.05.057>
- Zhang H, Li P, Hui N et al (2017a) The microstructure and methane catalytic combustion of ceria composite materials modified with tourmaline particles. *J Alloy Compd* 712:567–572. <https://doi.org/10.1016/j.jallcom.2017.04.140>
- Zhang K, Kim JK, Park B et al (2017b) Defect-induced epitaxial growth for efficient solar hydrogen production. *Nano Lett* 17:6676–6683. <https://doi.org/10.1021/acs.nanolett.7b02622>
- Zhao X, Lei Y, Fang P et al (2019) Piezotronic effect of single/few-layers MoS<sub>2</sub> nanosheets composite with TiO<sub>2</sub> nanorod heterojunction. *Nano Energy* 66:104168. <https://doi.org/10.1016/j.nanoen.2019.104168>
- Zhong W, Shen S, Feng S et al (2018) Facile fabrication of alveolate Cu<sub>2-x</sub>Se microspheres as a new visible-light photocatalyst for discoloration of rhodamine B. *Cryst Eng Comm* 20:7851–7856. <https://doi.org/10.1039/C8CE01534A>
- Zhou G, Liu H, Chen K et al (2018) The origin of pyroelectricity in tourmaline at varying temperature. *J Alloy Compd* 744:328–336. <https://doi.org/10.1016/j.jallcom.2018.02.064>
- Zhou Y, Fan X, Zhang G et al (2019) Fabricating MoS<sub>2</sub> nanoflakes photoanode with unprecedented high photoelectrochemical performance and multi-pollutants degradation test for water treatment. *Chem Eng J* 356:1003–1013. <https://doi.org/10.1016/j.cej.2018.09.097>